ACCSCIENCE PUBLISHING

International Journal of Bioprinting

RESEARCH ARTICLE

Collagen-sodium alginate-silk fibroin 3D-printed scaffold loaded with polydatin promotes cartilage regeneration by improving lipid metabolism and cell apoptosis

Weibin Du[1,2†*], Wenxiang Zeng[1,2†], Zhenwei Wang[1,2†], Huahui Hu[1,2], Yanghua Tang[1,2], Wei Zhuang[1,2], Guoping Cao[1,2] and Gang Qu[1,2*]

[1]Research Institute of Orthopedics, Jiangnan Hospital Affiliated to Zhejiang Chinese Medical University, Hangzhou, Zhejiang, China

[2]Hangzhou Xiaoshan Hospital of Traditional Chinese Medicine, Hangzhou, Zhejiang, China

(This article belongs to the *Special Issue: Bioprinting of Nanomaterials for Biomedical Applications*)

Abstract

Cartilage defects negatively impact the quality of life of over 500 million people worldwide. 3D-printed scaffolds loaded with polydatin (PD) have shown significant potential in cartilage defect repair. This study aims to investigate their reparative effects and analyze the associated metabolic changes using lipidomics techniques, providing new strategies for treating cartilage defects. Biocompatible 3D-printed scaffolds containing PD were prepared and 30 New Zealand rabbits were divided into three groups (10 rabbits per group) that underwent either sham surgery (Normal group) or surgical creation of a cartilage defect without scaffold filling (Model group) or with the developed scaffold filling (Scaffold group). After three months of intervention, the repair of cartilage defects was evaluated through macroscopic observation, micro-CT, hematoxylin and eosin (H&E) staining, and Safranin O/fast green (SFO/FG) staining. The expression of vascular endothelial growth factor A vascular endothelial growth factor A (VEGFA), Col2a1, and biglycan was detected by immunofluorescence while lipid metabolic profiling analysis was conducted on newly formed cartilage tissue to comprehensively evaluate the scaffold's mechanism of action. Macroscopic observation, micro-CT, H&E staining, and SFO/FG staining indicated that the repair of cartilage defects in the Scaffold group was significantly better than in the Model group, closely resembling the Normal group. Lipidomics revealed that the Scaffold group modulated 36 metabolites, with a recovery rate of 69.23%, including ceramides (Cers), glycerophospholipids (GPs), and sphingomyelins (SMs). Immunofluorescence analysis showed increased expression of cartilage cell markers Sox9, Col2a1, biglycan, and VEGFA, along with a reduction in cell apoptosis (all $p < 0.05$) after scaffold implantation. These findings collectively suggest that the PD-loaded 3D-printed scaffold promotes cartilage repair by restoring lipid metabolites in cartilage tissue, inhibiting chondrocyte apoptosis, enhancing vascular-related protein expression, and accelerating cartilage collagen matrix remodeling.

Keywords: 3D printing; Cartilage regeneration; Lipid metabolism; Cell apoptosis; Polydatin

[†]These authors contributed equally to this work.

***Corresponding authors:**
Gang Qu
(122653595@qq.com)

Weibin Du
(dwbbdm@163.com)

Citation: Du W, Zeng W, Wang Z, et al. Collagen-sodium alginate-silk fibroin 3D-printed scaffold loaded with polydatin promotes cartilage regeneration by improving lipid metabolism and cell apoptosis. *Int J Bioprint*. 2025;11(1):453-469. doi: 10.36922/ijb.6548

Received: November 23, 2024
1st revised: December 22, 2024
2nd revised: December 23, 2024
Accepted: December 24, 2024
Published Online: December 24, 2024

Copyright: © 2024 Author(s). This is an Open Access article distributed under the terms of the Creative Commons Attribution License, permitting distribution, and reproduction in any medium, provided the original work is properly cited.

Publisher's Note: AccScience Publishing remains neutral with regard to jurisdictional claims in published maps and institutional affiliations.

1. Introduction

Cartilage defects are often caused by osteoarthritis, injuries, or other factors, and have become a widespread condition globally, placing a heavy economic burden on healthcare systems and patients.[1,2] Cartilage defects negatively impact the quality of life for over 500 million people worldwide, and effective treatments have remained a significant challenge in clinical practice for nearly a decade.[3] Current treatment methods for cartilage defects, such as microfracture repair, high-density grafting, autologous and allogenic cartilage regeneration, and chondrocyte regeneration, can alleviate pain and enhance joint function.[4-7] However, the long-term clinical success rate beyond five years is poor, often necessitating total knee arthroplasty or revision surgeries for patients.[8,9] To overcome these challenges, osteochondral tissue engineering is a potentially promising solution. Through tissue engineering approaches, improved osteochondral regeneration protocols can be developed, effectively facilitating drug delivery.[10,11]

3D printing is a method for fabricating cartilage scaffolds that can be personalized, allowing for precise control of target structures.[12,13] Additionally, 3D printing technology can facilitate the delivery of cells, growth factors, or nanoparticles to injury sites, promoting cartilage regeneration for therapeutic purposes.[14,15] In our previous research, 3D printing technology has been repeatedly applied to achieve traumatic skin repair and drug delivery.[16,17] In this study, bioactive matrices were incorporated into the existing framework to enhance bioactivity, improve adhesion to growth plate chondrocytes, and support their growth while better aligning with the growth rate of tissue cells.

Polydatin (PD) is the active component of *Polygonum cuspidatum* and a glycoside derivative of resveratrol.[18] PD has demonstrated various biological benefits, with studies indicating its roles in bone metabolism regulation, anti-inflammatory effects, antioxidant properties, apoptosis regulation, and autophagy modulation.[19-21] Furthermore, research shows that PD can alleviate chondrocyte damage induced by inflammatory factors, and inhibit osteoclast formation and bone resorption, while also providing protection and repair for cartilage and subchondral bone.[19,22] However, there have been no studies applying PD to cartilage tissue engineering thus far.

Based on our group's pre-experiments and a review of relevant literature, we found that cartilage defect repair in rabbit knee joints reaches a critical stage at three months. At this time point, the overall condition of cartilage repair exhibits a notable contrast, leading most studies to select three months as the baseline for assessment and comparison. This period consistently demonstrates a more accurate reflection of the effects of cartilage repair compared to earlier time points.[23-25] Observations conducted either shorter or longer than three months may encounter incomplete or fully recovered cartilage repair, thereby diminishing the significance of inter-group comparisons.[26,27] Consequently, to enable a direct and meaningful comparison of the extent of cartilage repair, we established three months as the intervention time point to thoroughly investigate the mechanism by which the scaffold contributes to the cartilage repair process.

In this study, we developed a collagen-sodium alginate-silk fibroin 3D-printed scaffold loaded with PD to facilitate cartilage defect regeneration. We evaluated its compatibility with cartilage *in vitro* and assessed its efficacy in treating osteochondral defects in rabbits. Histopathological and lipidomic approaches were used to elucidate the mechanism of action underlying cartilage repair.

2. Methods

2.1. Experimental animals

Thirty male New Zealand white rabbits (2–3 kg) were grouped and acclimatized for one week at the Animal Experiment Center of Zhejiang Chinese Medical University before the experiment. The purchase and breeding of the New Zealand white rabbits, and other animal procedures followed the animal research guidelines set by the National Institutes of Health and the Animal Research Committee. Approval was obtained from the Animal Ethics Committee of Zhejiang Chinese Medical University (No. IACUC-20231030-14).

2.2 Preparation of 3D-printed scaffold loaded with PD

2.2.1. Preparation and sterilization of printing materials

While stirring, sodium alginate (Sigma, USA) and silk fibroin (Hefei Bomei Biotechnology Co., LTD, China), 0.8 g each, were dissolved in 8 L sterile phosphate-buffered saline (PBS) to make the printing material in solution state. The materials were loaded into a sealed container and subjected to intermittent sterilization at 70°C for 30 minutes each time, with a 24-hour interval between each session, for a total of three times. After these treatments, the materials were stored at 4°C for future use. Following these procedures, they were prepared as the 3D-printing substrate material.

2.2.2. Printing of scaffolds

Sodium alginate and silk fibroin were continuously printed and extruded into a flat dish using 3D bioprinting

technology (BioScaffolder, GeSiM, Germany) under the control of a computer-aided design (CAD) and a pneumatic pressure system. Immediately after printing, 5% calcium chloride was added to the scaffolds, and the scaffolds were instantly cross-linked and cured within the cross-linking solution. After curing, the scaffolds were washed with PBS and then transferred to petri dishes. The above steps were done in aseptic conditions. The printing parameters include a needle diameter of 0.41 mm, an extrusion air pressure of 120 kPa, a stent diameter of 6 mm, and a layer height of 2.4 mm. Each stent consisted of six layers, with each layer comprising six strips, printed at a 90° angle. The material was maintained at a heating temperature of 37°C throughout the process. Then, a mixture of 0.2% type I collagen (Hangzhou Xinyou Biotechnology Co., LTD, China) and 50 μM PD (Beijing Huawei Ruike Chemical Co., LTD, China) was added dropwise to the scaffolds. The petri dishes were then put into the incubator at 37°C for 2 hours to allow the collagen to change from liquid to gel. We arranged the above experimental steps and prepared a total of 20 scaffolds for backup.

2.3. Model preparation and grouping

Under inhalation anesthesia with isoflurane (Shanghai Yuyan Scientific Instrument Co., Ltd., China) at a rate of 0.4 mL/min, an incision was made along the inner edge of the patella, followed by careful separation of the subcutaneous tissue and incision of the medial joint capsule. The patella was dislocated laterally, and a hole was drilled at the center of the femoral trochlea in the rabbit knee joint using an electric drill, with a diameter of 5 mm and a depth of 3 mm, to create a cartilage defect model. The incision was then sutured layer by layer.

Using a random number table, 30 New Zealand rabbits were randomly divided into three groups, with ten rabbits in each group. The specific groupings were as follows: Normal group (sham surgery, no cartilage damage); Model group (surgical creation of cartilage defect model, no scaffold filling); Scaffold group (surgical creation of cartilage defect, filled with a 3D-printed scaffold containing PD, with scaffold preparation following the protocol established by our research group previously[16]). The distal femur was collected for analysis after three months. The experimental scheme is shown in Figure 2a.

2.4. Cell viability test

Cell viability was evaluated using the Cell Counting Kit-8 (CCK-8) method. To evaluate the optimal concentration of PD, chondrocytes were first evenly plated in a 96-well plate at a density of 1×10^4 cells per well and cultured for 24 hours. Different concentrations (10, 20, 50, 100, and 200 μM) of PD were added, and after 24 hours, 10 μL of CCK-8 solution (Hangzhou Nuoyang Bio-Technology Co., LTD, China) was added to each well. The plate was then incubated at 37°C in a 5% CO_2 incubator for 2 hours. The optical density (OD) value of absorbance was measured at a wavelength of 450 nm using a microplate reader (Bio-Rad, USA).

To evaluate the effect of PD scaffolds on cell viability, 1×10^4 chondrocytes were cultured on empty plates (blank), non-PD scaffolds (control group), and scaffolds containing PD (experimental group). Then 10 μL CCK-8 solution was added at 12, 24, 36, 48, 60, 72, and 84 hours. The plates were then incubated and the OD value of absorbance was measured as described above. Finally, the cell viability value was calculated according to the following formula: Cell viability (%) = [(OD value of experimental group − OD value of blank)/(OD value of control group − OD value of blank)] × 100%.

2.5. Measurement of scaffold water absorption and expansion rate

Three lyophilized scaffolds were each added to 1 mL of physiological saline and placed on a shaker at 37°C and 135 rpm/min. The scaffolds were removed every 30 minutes, surface moisture was dried, and the mass of the scaffolds after water absorption was measured, with observations continuing for 3 hours. The water absorption expansion rate was calculated using the following formula: Water absorption expansion rate (%) = [(mass of the scaffold after absorption − dry mass of the scaffold)/dry mass of the scaffold] × 100%.

2.6. TUNEL detection

A scaffold was placed in a 24-well plate, and 1×10^4 cells were seeded onto the scaffold. After 48 hours, the scaffold was removed and observed under a microscope for imaging. The scaffold was then fixed in 4% paraformaldehyde (Wuhan Servicebio Technology CO., LTD, China) for 20 minutes and permeabilized with 0.5% Triton X-100 (Wuhan Servicebio Technology CO., LTD, China) for 10 minutes. Subsequently, the TUNEL apoptotic assay (Wuhan Servicebio Technology CO., LTD, China) was performed according to the manufacturer's instructions, followed by 4', 6-diamidino-2-phenylindole (DAPI) nuclear staining. Finally, stereoscopic images were captured under laser confocal microscopy (Nikon, Japan). The distal femoral tissue of rabbits was fixed in 4% paraformaldehyde, decalcified in 10% Ethylene Diamine Tetraacetic Acid (EDTA), dehydrated through a graded alcohol series, embedded in paraffin, and sectioned at 5 μm. The sections were permeabilized with 0.5% Triton X-100 for 10 minutes, followed by TUNEL apoptotic assay (Wuhan Servicebio Technology CO., LTD, China) and DAPI staining. Imaging was performed under a fluorescence microscope.

2.7. Scanning electron microscopy observation

The 3D-printed scaffold containing PD was fixed overnight at 4°C in a 2.5% glutaraldehyde solution (Hangzhou Nuoyang Biotechnology Co., LTD, China). After fixation with 1% osmium tetroxide (Hangzhou Nuoyang Biotechnology Co., LTD, China), the samples underwent dehydration through graded concentrations of ethanol (30, 50, 70, 80, 90, and 100%). They were then treated with a mixture of ethanol and isopropyl acetate, followed by critical point drying and platinum sputtering, and subsequently observed under a scanning electron microscope.

2.8. Histopathological examination

The distal femoral tissue of rabbits was fixed in 4% paraformaldehyde, decalcified in 10% EDTA, dehydrated through a graded alcohol series, and embedded in paraffin. Sections (5 μm) were stained with hematoxylin and eosin (H&E) and Safranin O/fast green (SFO/FG), and observed under a microscope after being mounted with neutral resin.

2.9. Micro-CT detection

The rabbit femur was obtained, and the distal soft tissue was removed. After fixation in paraformaldehyde for 48 hours, it was preserved in a 75% ethanol solution. Micro-CT scans (Skyscan1176, Bruker micro-CT N.V., Kontich, Belgium) were performed on the distal femur to create 3D images, allowing for the observation of microstructural changes in the modeling area.

2.10. UHPLC-QTOF/MS pre-treatment of cartilage tissue

Rabbit cartilage tissue was crushed in liquid nitrogen and 30 mg was added to ten times its volume of isopropanol and vortexed for 1 minute. After ice bath sonication for 30 minutes, the sample was vortexed again for 1 minute and left overnight at −20°C. The following day, the centrifuge was pre-cooled to 4°C and centrifuged at 13,000 rpm for 15 minutes. The supernatant (200 μL) containing cartilage tissue was nitrogen-blown to dryness, reconstituted in 100 μL of isopropanol, and centrifuged at 13,000 rpm for 15 minutes, with 80 μL of supernatant placed in an injection vial for analysis. An equal amount was homogenized, centrifuged, nitrogen-dried, and reconstituted to prepare quality control (QC) samples.

2.11. Liquid chromatography and mass spectrometry

The following conditions were used for liquid chromatography and mass spectrometry: Column: Waters Acquity BEH C18 column (2.1 × 100 mm, 1.7 μm); Column temperature: 55°C; Mobile phase A: water-acetonitrile (40:60, containing 0.1% formic acid and 5 mM ammonium formate); Mobile phase B: isopropanol-acetonitrile (90:10, containing 0.1% formic acid and 5 mM ammonium formate); Flow rate: 0.3 mL/min; Injection volume: 2 μL. The samples were analyzed using a SCIEX Exion LC coupled with an X500B QTOF mass spectrometer (AB Sciex, Foster City, CA, USA). Electrospray ionization (ESI) was used in positive and negative ion scanning modes, with a scanning range of m/z 150–1050.

2.12. Data preprocessing

The raw data was filtered using MarkerView 1.3.1 software (AB Sciex, Foster City, CA, USA), and a data matrix transformation was performed, primarily including information on the mass-to-charge ratio (m/z), retention time (Rt), and peak area (intensity). After normalizing all data using the total peak area, an Excel table was generated for subsequent lipidomics analysis. To reduce signal interference from random errors, variables in QC with relative standard deviation RSD ≥40% were initially removed in Excel. The Excel file was then imported into SIMCA 14.1 (Umetrics, Umeå, Sweden) for multivariate statistical analysis. Finally, partial least squares discriminant analysis (PLS-DA) was conducted on all groups to observe the overall metabolic profile changes of all samples, with permutation tests used to validate model overfitting.

2.13. Differential metabolite analysis

Orthogonal partial least squares discriminant analysis (OPLS-DA) was further used to screen for differential variables between Normal and Model groups. The screening criteria were: Variable Importance in Projection VIP ≥1 and |pcorr| ≥0.4. The selected variables were subjected to significance testing using the Mann-Whitney test, with a p-value ≤0.05 indicating significant differential variables. Fold change (FC) was calculated, with FC (Model / Normal) plotted on the x-axis and p-value as the y-axis to create a volcano plot. Variables farther from the origin indicate greater differential contribution, with red indicating significant upregulation post-modeling (FC >1.5), blue indicating significant downregulation (FC < 0.67), and gray indicating no difference.

2.14. Immunofluorescence detection

Femoral tissue was fixed in 4% paraformaldehyde, decalcified in 10% EDTA, and then embedded in paraffin before slicing (5 μm). After dewaxing and rehydrating, antigen retrieval was performed, followed by permeabilization with 0.5% Triton X-100 for 10 minutes. Primary antibodies of SRY-box transcription factor 9 (Sox9) (1:500), vascular endothelial growth factor A (VEGFA) (1:500), (Collagen Type II Alpha 1) Col2 (1:500), and biglycan (1:500) (Beijing, Boaoson Biotechnology Co., Ltd, China) were prepared. The primary antibodies were incubated together with the fluorescent secondary antibodies, followed by mounting with a DAPI-containing

mounting medium. Images were captured using a fluorescence microscope.

2.15. Statistical analysis

All experimental results were expressed as mean ± SD (standard deviation). All statistical analyses were performed using SPSS 21.0 software (IBM, China). A p-value of less than 0.05 was considered statistically significant.

3. Results

3.1. PD-collagen-sodium alginate-silk fibroin 3D-printed scaffold is compatible with chondrocyte

To screen for the most suitable PD concentration for chondrocyte growth, we identified 50 μM as the optimal concentration through the CCK-8 assay (Figure 1a). The 3D-printed scaffold containing PD is transparent and exhibits good formability, uniform pore size, consistent spacing, and even thickness, as well as good water absorption and swelling properties (Figures 1b and c). In addition, we used CCK-8 to screen the effects of different scaffolds on cell proliferation and found that scaffolds containing PD components had a significant impact on chondrocyte proliferation (Figure 1d). When chondrocytes were seeded onto the scaffold, we observed that the cells adhered and grew around the voids. In TUNEL assays, only a small number of cells seeded onto the scaffold were found to be apoptotic (Figure 1e). Scanning electron microscopy revealed numerous protrusions around the scaffold pores, which are beneficial for cell adhesion (Figure 1f). After cell implantation, we found that the cells were able to adhere and grow stably on the scaffold (Figure 1g). These results indicate that the PD-collagen-sodium alginate-silk fibroin 3D-printed scaffold has good cell compatibility, facilitating cell adhesion and growth.

3.2. Implantation of PD-collagen-sodium alginate-silk fibroin 3D-printed scaffold in defected rabbit cartilage promotes cartilage repair

To verify the scaffold's effects on cartilage *in vivo*, we established a distal femoral cartilage defect model in rabbits and implanted the scaffold at the defect site (Figure 2b). Three months post-implantation, we harvested the distal femur of the rabbits and found that the cartilage defect was better repaired under the scaffold's influence compared to the Model group (Figure 2c). Subsequently, histopathological examinations showed that good cartilage repair was evident under H&E and SFO/FG staining after scaffold implantation (Figures 2d and e). Additionally, micro-CT analysis of the harvested femur indicated that the cartilage defect area post-implantation was closer to that of the Normal group compared to the Model group (Figure 2f). Collectively, these results show that the implantation of the scaffold improved the repair of the cartilage defect in the distal femur of rabbits.

3.3. Repeatability and stability of the UHPLC-QTOF/MS method

Figures 3a and b present the overlaid QC plots under positive and negative ion modes. The spectra are almost entirely overlapping, indicating that the data obtained is stable and reliable. The principal component analysis (PCA) plots for all samples under negative and positive ion modes are shown in Figures 3c and d, respectively. The QC samples cluster tightly, suggesting good stability and repeatability of the experiment. Moreover, the Normal, Model, and Scaffold groups are distinctly separated, with the Scaffold group positioned in between, indicating significant changes in the lipid profile of the Model group post-modeling, and that treatment can partially revert these changes. Further analysis using PLS-DA for all groups is illustrated in Figures 3e–h, where clear distinctions among the three groups are observed; the Scaffold group is positioned between the Normal and Model groups, suggesting that the lipid profile in the Scaffold group is shifting toward recovery.

3.4. Differential metabolite analysis results

Figures 4a–d show the OPLS-DA results for the Normal group versus the Model group, indicating a difference between the two groups and confirming the validity of the model. Figure 4e presents a volcano plot for both models, where variables further from the origin indicate greater differential contributions, with red signifying significant upregulation post-modeling, blue indicating significant downregulation, and gray showing no differences. Subsequently, differential variables were filtered and annotated, as seen in Table 1. A total of 52 differential metabolites were identified, primarily consisting of ceramides (Cers), glycerophospholipids (GPs), sphingomyelins (SMs), and triglycerides (TGs). The scaffold group showed a recovery of 36 metabolites, with a recovery rate of 69.23%. The Venn diagram illustrating the differential metabolites identified in all three groups is shown in Figure 4f. The heatmap of the 52 differential metabolites is illustrated in Figure 4g, where red indicates high response and blue indicates low response. Differences between Normal and Model groups are evident, with some recovery in the Scaffold group—particularly notable in the Cers. The fold changes ($\log_2$) of the 36 recovered metabolites in the Model (compared to Normal group) and Scaffold (compared to the Model group) groups are presented in Figure 4h, showing that these metabolites, mainly Cers, GPs, and SMs, were generally decreased in the Model group but significantly increased after treatment.

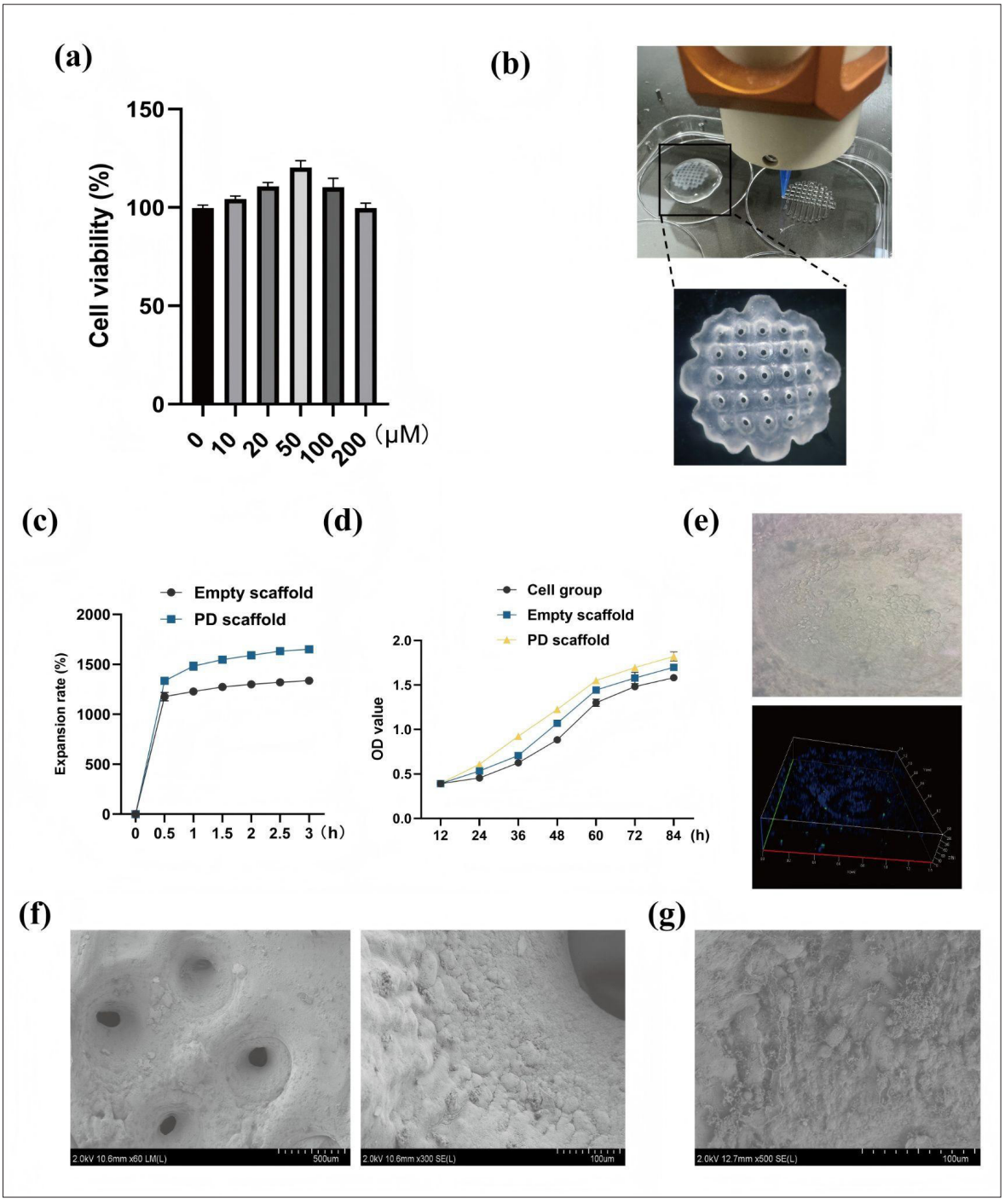

Figure 1. Preparation and evaluation of PD-collagen-sodium alginate-silk fibroin 3D-printed scaffold and its chondrocyte compatibility. (a) CCK-8 assay screening for optimal concentration of PD for chondrocyte growth; (b) Images of the 3D printing procedure and the resulting scaffold structure; (c) Water absorption and swelling rates of the scaffold; (d) CCK-8 assay comparing the effects of different scaffolds on cell proliferation; (e) Microscopic images showing chondrocytes growing around the scaffold pore size (magnification ×50), with TUNEL staining showing blue for cell nuclei and green for apoptotic (TUNEL positive) cells (magnification ×10); (f) Scanning electron microscopy images of the scaffold surface (magnification ×60 and ×300); and (g) Visualization of cells growing on the scaffold (magnification ×500). Abbreviations: CCK-8: Cell Counting Kit-8; PD: Polydatin; OD: Optical density.

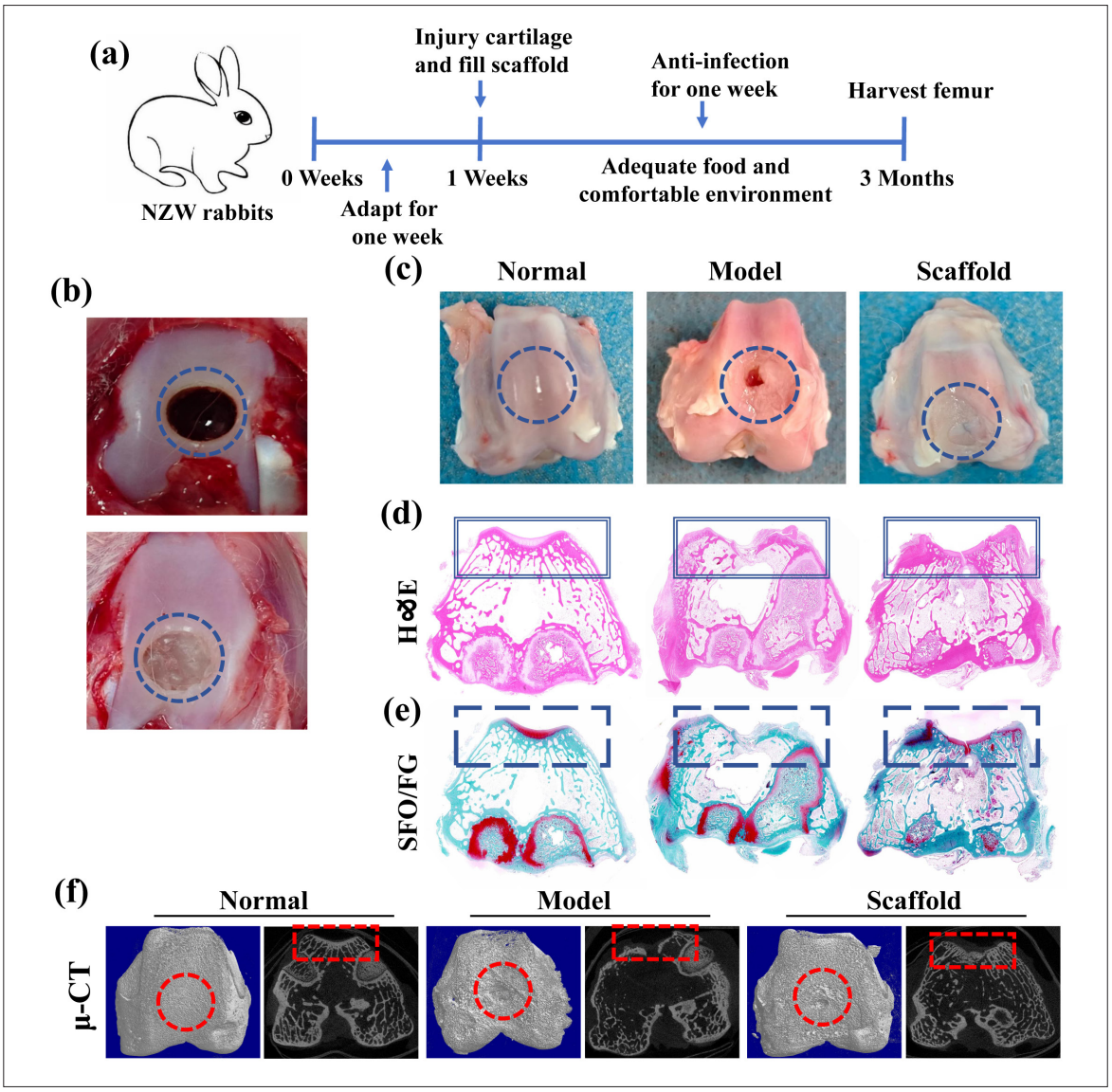

Figure 2. Scaffold implantation in rabbit cartilage defects facilitates cartilage repair. (a) Experimental workflow for animal study; (b) Images of cartilage defects before and after scaffold implantation; (c) Macroscopic appearance of the distal femur after three months post-implantation, with circles indicating defect sites (magnification × 1); (d) H&E staining of the distal femur, with rectangles indicating defect sites (magnification × 1); (e) SFO/FG staining of the distal femur, with rectangles indicating defect sites (magnification × 1); and (f) Micro-CT imaging of the distal femur, with circles indicating 3D defect sites and rectangles indicating 2D defect sites (magnification × 1). Abbreviations: H&E: Hematoxylin and eosin; NZW: New Zealand; SFO/FG: Safranin O/fast green.

The TG compounds were elevated in the Model group but were not regulated by the treatment group.

3.5. Implantation of scaffolds promotes the proliferation of chondrocytes, angiogenesis, and collagen matrix remodeling

TUNEL and immunofluorescence assays were performed on tissues from the distal femur modeling area across the three groups. After scaffold implantation, the number of apoptotic cells significantly decreased compared to the model group (Figures 5a and b). Additionally, immunofluorescence results indicated that, after scaffold implantation, the expression of Sox9, VEGFA, Col2a1, and biglycan in the damaged local area significantly reverted, becoming closer to the normal group (Figures 5c–g). These results suggest that scaffold implantation is beneficial for chondrocyte proliferation, angiogenesis, and collagen matrix remodeling. Finally,

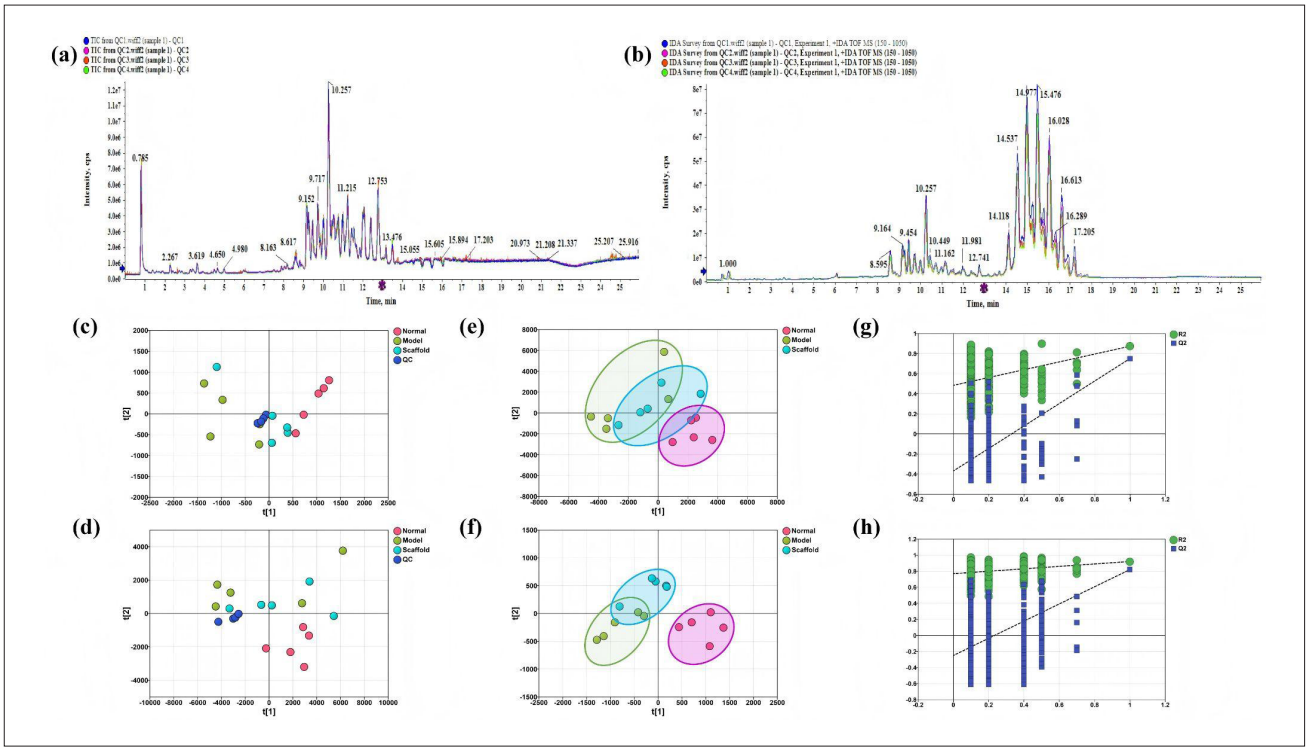

Figure 3. QC sample BPC overlay and data quality assessment in negative and positive ion modes. (a) Negative ion mode; (b) Positive ion mode. Data quality assessment: (c) PCA scatter plot for negative ion mode (R^2X = 0.846, Q^2 = 0.663); (d) PCA scatter plot for positive ion mode (R^2X = 0.916, Q^2 = 0.803); (e) PLS-DA scatter plot for negative ion mode (R^2X = 0.873, R^2Y = 0.940, Q^2 = 0.710); (f) PLS-DA scatter plot for positive ion mode (R^2X = 0.914, R^2Y = 0.858, Q^2 = 0.537); (g) PLS-DA negative ion permutation test; and (h) PLS-DA positive ion permutation test. Abbreviations: BPC: Base peak chromatogram; QC: Quality control; PCA: Principal component analysis; PLS-DA: Partial least squares discriminant analysis.

based on lipidomics techniques and immunofluorescence results, along with Kyoto Encyclopedia of Genes and Genomes (KEGG) pathway analysis and literature reviews, a schematic diagram (Figure 6) was created to explore the potential mechanism of action of the PD-collagen-sodium alginate-silk fibroin 3D-printed scaffold in rabbit cartilage defect repair.

4. Discussion

Due to the poor self-repair capability of natural cartilage, effective treatment options for cartilage repair are limited. Tissue engineering offers a promising alternative for tissue replacement, particularly through the development of scaffolds that can provide localized delivery, are tissue-compatible, and effectively promote tissue regeneration. To achieve these characteristics, we prepared a collagen-sodium alginate-silk fibroin 3D-printed scaffold loaded with PD to promote cartilage regeneration. Collagen is the most abundant protein in the human body and a component of the extracellular matrix (ECM), possessing unique strength and toughness suitable for the regeneration of various tissues, including bone, cartilage, and skin.[28] Silk fibroin is a natural protein containing essential amino acids, known for its good biocompatibility, unique mechanical properties, excellent processability, and degradability.[29] Sodium alginate, a natural polysaccharide extracted from brown algae, is commonly used in tissue engineering materials and enhances the drug release and rapid solidification capabilities of scaffolds.[30,31] The incorporation of silk fibroin and sodium alginate into collagen effectively improves the degradation rate and enhances its adhesion to growth plate chondrocytes, supporting cell growth and better matching the growth rate of tissue cells.

Our group has been investigating these matrix materials for an extended period, and preliminary studies have indicated that these materials exhibit favorable biocompatibility *in vivo*, without significant immune rejection or inflammatory responses.[17] In this study, after 3D printing, we prepared a porous scaffold with good water absorption and swelling properties. Chondrocytes were seeded onto the scaffold, demonstrating good cell compatibility and promoting cell adhesion and growth. Subsequently, the scaffolds were implanted into rabbit cartilage defects, resulting in satisfactory repair of the defect area. Lipidomics analysis revealed that 36 metabolites were restored in the scaffold group, achieving a recovery rate

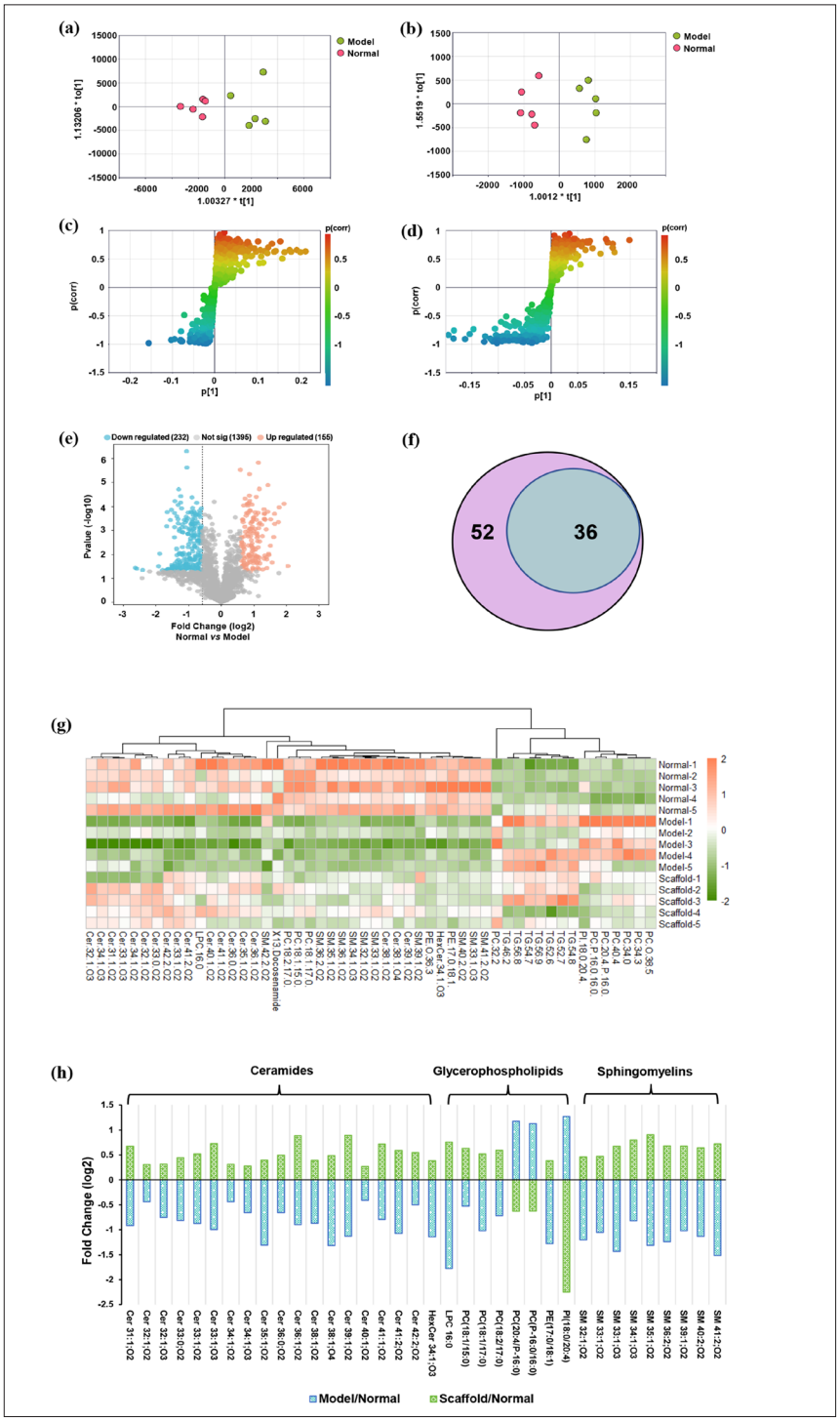

Figure 4. Analysis of differential metabolites. (a) OPLS-DA scatter plot for Model vs. Normal in negative ion mode (R^2X 0.668, R^2Y 0.951, Q^2 0.765); (b) Negative ion S-plot; (c) OPLS-DA scatter plot for Model vs. Normal in positive ion mode (R^2X 0.824, R^2Y 0.866, Q^2 0.779); (d) Positive ion S-plot; R^2X and R^2Y display the fraction of the sum of squares for the selected component, i.e. what percentage of the information in the original data is explained by the model through principal components. Q^2: The fraction of the total variation of X or Y that can be predicted by a component, as estimated by cross-validation. (e) Volcano plot highlighting metabolites with p-value ≤0.05 and fold change (Model/Normal) >1.5 (upregulated; red dots) or <0.67 (downregulated; blue dots); (f) Venn diagram showing overlap among differential metabolites; (g) Heatmap of 52 differential metabolites; and (h) Log_2 fold change of 36 everted metabolites, indicating recovery trends in the Scaffold group. Abbreviations: OPLS-DA: Orthogonal partial least squares discriminant analysis.

Table 1. Differential metabolites across groups

No.	Metabolites	Formula	rt	Ion mode	m/z	VIP	p(corr)	p	p	FC	FC	Regulated
								M vs N	S vs M	M/N	S/M	
1	LPC 16:0	$C_{24}H_{50}NO_7P$	2.29	M+H	496.3400	1.05	−0.79	0.0283	0.0283	0.74	1.24	√
2	13-Docosenamide	$C_{22}H_{43}NO$	6.12	M+H	338.3411	2.16	−0.77	0.0472	0.1172	0.48	1.31	—
3	SM 32:1;O2	$C_{37}H_{75}N_2O_6P$	7.95	M+H	675.5424	1.01	−0.97	0.0090	0.0283	0.42	1.60	√
4	SM 33:1;O3	$C_{38}H_{77}N_2O_7P$	8.20	M+H	705.5539	1.38	−0.94	0.0090	0.0090	0.35	1.65	√
5	PC 32:2	$C_{40}H_{76}NO_8P$	8.54	M+H	730.5432	1.06	0.74	0.0090	0.7540	1.28	0.94	—
6	Cer 31:1;O2	$C_{31}H_{61}NO_3$	8.55	M+FA−H	540.4607	1.04	−0.82	0.0090	0.0472	0.50	1.65	√
7	PC 34:3	$C_{42}H_{78}NO_8P$	8.60	M+H	756.5506	1.27	0.73	0.0283	0.1745	1.64	0.78	—
8	SM 33:1;O2	$C_{38}H_{77}N_2O_6P$	8.61	M+H	689.5573	4.23	−0.98	0.0090	0.0163	0.48	1.51	√
9	Cer 32:1;O3	$C_{32}H_{63}NO_4$	8.71	M+FA−H	570.4739	1.12	−0.75	0.0163	0.0472	0.58	1.65	√
10	SM 34:1;O3	$C_{39}H_{79}N_2O_7P$	8.79	M+H	719.5689	2.21	−0.93	0.0090	0.0090	0.55	1.31	√
11	Cer 32:1;O2	$C_{32}H_{63}NO_3$	9.17	M+FA−H	554.4784	1.82	−0.63	0.0472	0.0472	0.71	1.46	√
12	HexCer 34:1;O3	$C_{40}H_{77}NO_9$	9.22	M+FA−H	760.5595	1.31	−0.90	0.0090	0.0472	0.43	1.37	√
13	PI(18:0/20:4)	$C_{47}H_{83}O_{13}P$	9.24	M−H	885.5501	2.02	0.69	0.0472	0.0163	2.41	0.21	√
14	Cer 33:1;O3	$C_{33}H_{65}NO_4$	9.27	M+FA−H	584.4906	2.45	−0.87	0.0090	0.0472	0.49	1.59	√
15	SM 36:2;O2	$C_{41}H_{81}N_2O_6P$	9.27	M+FA−H	773.5767	1.25	−0.90	0.0090	0.0472	0.41	1.30	√
16	PC(20:4/P-16:0)	$C_{44}H_{80}NO_7P$	9.67	M+FA−H	810.5662	1.77	0.78	0.0090	0.0283	2.26	0.65	√
17	Cer 33:1;O2	$C_{33}H_{65}NO_3$	9.73	M+H	524.5035	1.39	−0.88	0.0090	0.0090	0.54	1.85	√
18	PC(18:1/15:0)/ PC(16:0/17:1)	$C_{41}H_{80}NO_8P$	9.75	M+FA−H	790.5570	2.66	−0.94	0.0090	0.0472	0.63	1.21	√
19	SM 35:1;O2	$C_{40}H_{81}N_2O_6P$	9.77	M+H	717.5884	2.15	−0.94	0.0090	0.0283	0.40	1.40	√
20	PC(18:2/17:0)	$C_{43}H_{82}NO_8P$	9.8	M+FA−H	816.5747	1.15	−0.93	0.0090	0.0472	0.59	1.25	√
21	Cer 34:1;O3	$C_{34}H_{67}NO_4$	9.84	M+FA−H	598.5049	2.66	−0.86	0.0090	0.0472	0.63	1.41	√
22	PC O-38:5	$C_{46}H_{84}NO_7P$	9.85	M+H	794.6033	1.12	0.76	0.0283	0.2506	2.01	0.68	—
23	Cer 33:0;O2	$C_{33}H_{67}NO_3$	10.07	M+FA−H	570.5101	1.07	−0.79	0.0163	0.0472	0.57	1.74	√
24	Cer 34:1;O2	$C_{34}H_{67}NO_3$	10.25	M+FA−H	582.5100	5.06	−0.76	0.0163	0.0472	0.74	1.24	√
25	SM 36:1;O2	$C_{41}H_{83}N_2O_6P$	10.31	M+H	731.6068	2.79	−0.92	0.0090	0.0758	0.47	1.32	—
26	PC(P-16:0/16:0)	$C_{40}H_{80}NO_7P$	10.66	M+FA−H	762.5645	1.24	0.83	0.0090	0.0472	2.19	0.65	√
27	PC(18:1/17:0)	$C_{43}H_{84}NO_8P$	10.73	M+FA−H	818.5912	2.53	−0.98	0.0090	0.0163	0.48	1.39	√

(Continued ...)

Table 1. (*Continued ...*)

No.	Metabolites	Formula	rt	Ion mode	m/z	VIP	p(corr)	p	p	FC	FC	Regulated
								M vs N	S vs M	M/N	S/M	
28	Cer 35:1;O2	$C_{35}H_{69}NO_3$	10.76	M+H	552.5343	1.27	−0.96	0.0090	0.0090	0.40	1.87	√
29	PC 40:4	$C_{48}H_{88}NO_8P$	10.88	M+H	838.6280	1.00	0.83	0.0283	0.1172	2.32	0.65	—
30	PE(17:0/18:1)	$C_{40}H_{78}NO_8P$	10.96	M−H	730.5408	1.36	−0.96	0.0090	0.0472	0.40	1.32	√
31	PE O-36:3	$C_{41}H_{78}NO_7P$	11.05	M+H	728.5584	1.54	−0.91	0.0090	0.9168	0.65	1.03	—
32	PC 34:0	$C_{42}H_{84}NO_8P$	11.11	M+H	762.5997	1.66	0.78	0.0283	0.1745	2.57	0.60	—
33	SM 40:2;O2	$C_{45}H_{89}N_2O_6P$	11.15	M+H	785.6518	1.43	−0.92	0.0090	0.0472	0.45	1.30	√
34	Cer 36:1;O2	$C_{36}H_{71}NO_3$	11.24	M+H	566.5495	1.57	−0.89	0.0090	0.0163	0.53	1.59	√
35	Cer 36:0;O2	$C_{36}H_{73}NO_3$	11.54	M+FA−H	612.5558	1.16	−0.82	0.0090	0.0090	0.61	1.51	√
36	SM 41:2;O2	$C_{46}H_{91}N_2O_6P$	11.58	M+H	799.6646	2.09	−0.95	0.0090	0.0163	0.29	1.69	√
37	SM 39:1;O2	$C_{44}H_{89}N_2O_6P$	11.62	M+FA−H	817.6432	1.38	−0.93	0.0090	0.0090	0.49	1.44	√
38	Cer 38:1;O4	$C_{38}H_{75}NO_5$	11.65	M+FA−H	624.5559	2.57	−0.93	0.0090	0.0472	0.37	1.59	√
39	SM 42:2;O2	$C_{47}H_{93}N_2O_6P$	12.01	M+H	813.6844	1.41	−0.64	0.0472	0.7540	0.74	0.98	—
40	Cer 38:1;O2	$C_{38}H_{75}NO_3$	12.07	M+FA−H	638.5713	2.89	−0.92	0.0090	0.0090	0.55	1.43	√
41	Cer 41:2;O2	$C_{41}H_{79}NO_3$	12.38	M+H	634.6130	1.60	−0.95	0.0090	0.0090	0.46	1.86	√
42	Cer 39:1;O2	$C_{39}H_{77}NO_3$	12.45	M+FA−H	652.5879	2.51	−0.92	0.0090	0.0163	0.46	1.56	√
43	Cer 42:2;O2	$C_{42}H_{81}NO_3$	12.73	M+H	648.6278	1.56	−0.83	0.0163	0.0090	0.69	1.55	√
44	Cer 40:1;O2	$C_{40}H_{79}NO_3$	12.80	M+FA−H	666.6035	2.18	−0.80	0.0090	0.0090	0.75	1.20	√
45	Cer 41:1;O2	$C_{41}H_{81}NO_3$	13.15	M+FA−H	680.6168	2.36	−0.86	0.0090	0.0090	0.57	1.36	√
46	TG 56:8	$C_{59}H_{98}O_6$	14.35	M+NH4	920.7663	1.60	0.69	0.0472	0.6015	3.42	0.74	—
47	TG 46:2	$C_{49}H_{90}O_6$	14.39	M+NH4	792.7043	1.49	0.70	0.0472	0.4647	2.71	0.67	—
48	TG 52:7	$C_{55}H_{92}O_6$	14.41	M+H	849.6933	1.03	0.84	0.0283	0.6015	1.57	0.96	—
49	TG 56:9	$C_{59}H_{96}O_6$	14.54	M+H	901.7253	1.78	0.70	0.0472	0.4647	1.51	0.94	—
50	TG 54:8	$C_{57}H_{94}O_6$	14.58	M+H	875.7112	1.72	0.81	0.0283	0.7540	1.50	0.97	—
51	TG 54:7	$C_{57}H_{96}O_6$	15.02	M+H	877.7256	1.60	0.78	0.0283	0.3472	1.32	0.96	—
52	TG 52:6	$C_{55}H_{94}O_6$	15.16	M+H	851.7134	1.00	0.71	0.0472	0.6015	1.29	0.91	—

Abbreviations: Cer: Ceramide; Col2a1: Collagen Type II Alpha 1; CDP: Cytidine-diphosphate; ECM: Extracellular matrix; LPC: Lysophosphatidylcholine; M vs N: Model versus Normal; S vs M: Scaffold versus Model; m/z: Mass-to-charge ratio, m is the standard proton mass and z is the charged particle; PE: Phosphatidyl ethanolamine; PC: Phosphatidylcholine; p(corr): Correlation coefficient, the correlation coefficient between the sample score and the variable; Sox9: SRY-box transcription factor 9; FA: Fatty acid; FC: Fold change; SM: Sphingomyelins; SMS: SM synthase; Rt: Retention time; TG: Triglycerides; VIP: Variable importance in projection.

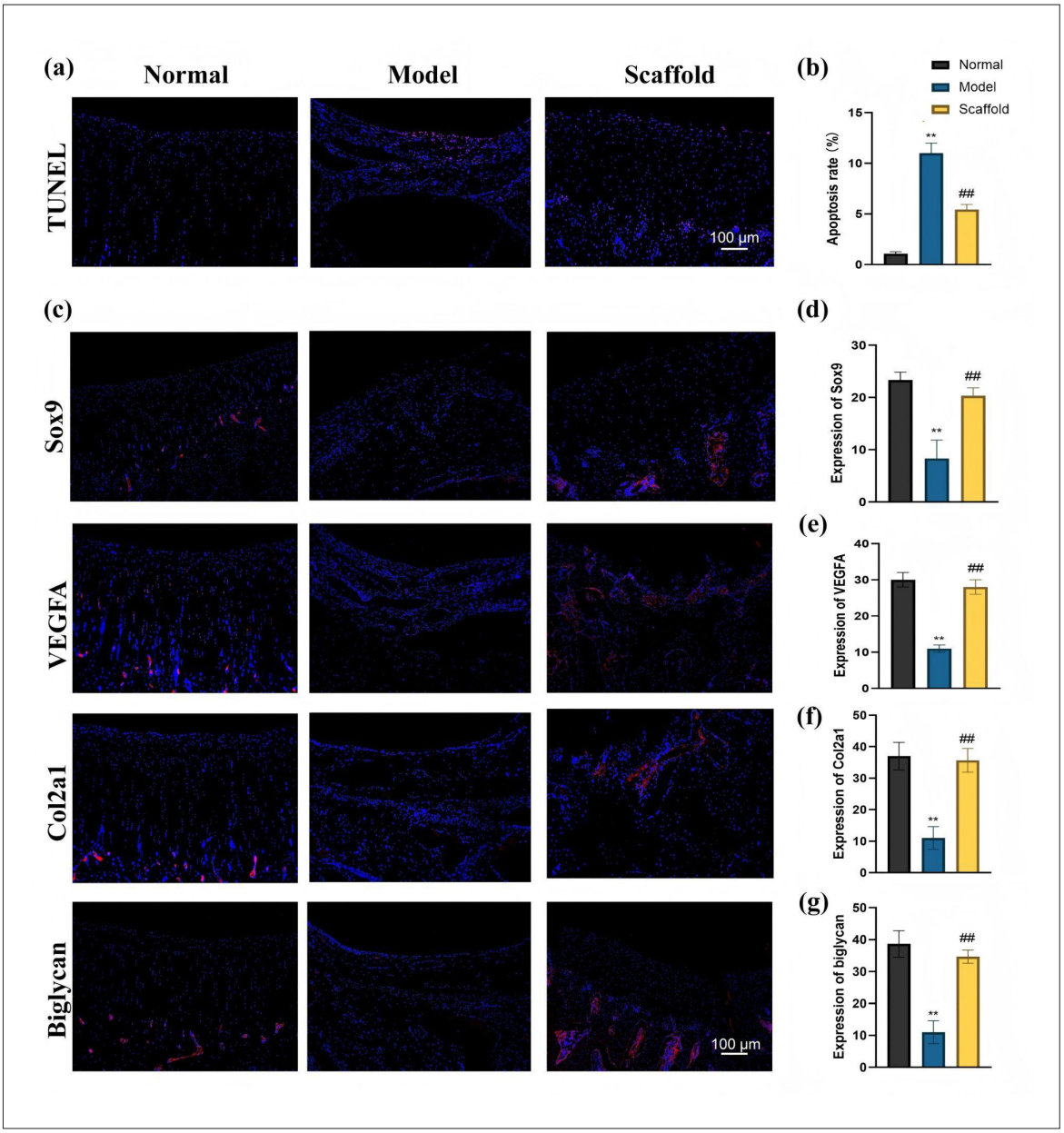

Figure 5. Scaffold implantation promotes chondrocyte proliferation, angiogenesis, and matrix stabilization. (a) TUNEL detection in rabbit distal femur, with blue indicating cell nuclei and green indicating TUNEL-positive cells; (b) Quantitative statistics of TUNEL-positive cells in different groups; (c) Immunofluorescence detection of Sox9, VEGFA, Col2a1, and biglycan expression, with blue indicating cell nucleus and red indicating positive expression sites; and (d–g) Quantitative statistics of Sox9, VEGFA, Col2a1, and biglycan expression based on immunofluorescence data. Data are expressed as mean ± SD. ns, no statistical significance; *p <0.05, **p <0.01 compared to Normal group; # p <0.05, ## p <0.01 compared to Model group, n = 5 per group. Abbreviations: Col2a1: Collagen Type II Alpha 1; Sox9: SRY-box transcription factor 9; SD: Standard deviation; VEGFA: Vascular endothelial growth factor A.

of 69.23%. The main metabolites recovered were Cers, GPs, and SMs. Furthermore, after scaffold implantation, immunofluorescence showed increased expression of Sox9, Col2a1, biglycan, and VEGFA in chondrocytes, along with a reduction in cell apoptosis.

Cer is a class of lipid molecules present in cell membranes that play a crucial role in regulating cellular functions and signal transduction.[32] Cer is involved in processes such as apoptosis (programmed cell death), inflammatory responses, and cellular stress. They also play

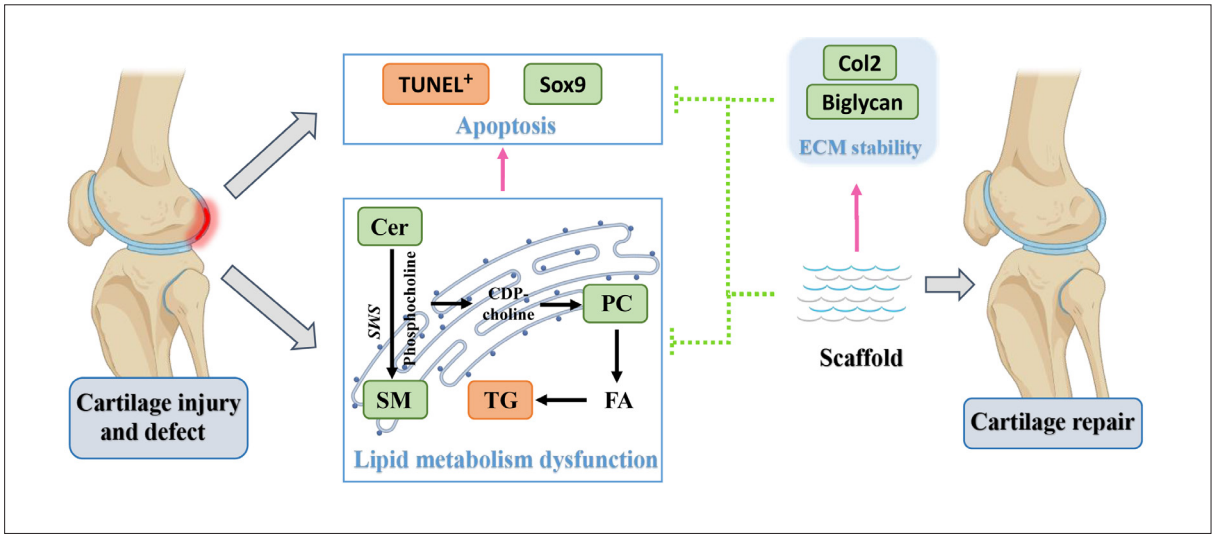

Figure 6. Diagram of cartilage injury and repair mechanisms. The green box indicates metabolites decreased after cartilage injury, while the orange box indicates metabolites increased. Green text indicates biochemical markers that decrease after cartilage injury, while orange text indicates those that increase. Red arrows indicate stimulation and green arrows indicate inhibition. Abbreviations: Cer: Ceramide; Col2a1: Collagen Type II Alpha 1; CDP: Cytidine-diphosphate; ECM: Extracellular matrix; PC: Phosphatidylcholine; Sox9: SRY-box transcription factor 9; FA: Fatty acid; SM: Sphingomyelins; SMS: SM synthase; TG: Triglycerides.

a key role in regulating membrane fluidity, signaling, and metabolism.[33] In apoptosis and inflammatory response research, Ye et al.[21] found that PD could improve the pathological injury of rat knee cartilage tissue and inhibit apoptosis in knee osteoarthritis. This mechanism of action may be through the regulation of autophagy mediated by the Adenosine Monophosphate-Activated Protein Kinase/Mammalian Target of Rapamycin (AMPK/mTOR) signaling pathway. Another study pointed out that PD could have a protective effect on knee cartilage by inhibiting nuclear factor kappa B (NF-κB) and Wnt/β-catenin signaling pathways and reducing the occurrence of inflammation.[34] These research results were a key factor in our research group selecting PD as the intervention method and may also represent one of the mechanisms of PD's action in this study. Both apoptosis and inflammatory reactions are closely related to the fluctuation of Cer levels. Most studies focus on the relationship between increased Cer levels and cartilage damage, indicating that elevated Cer is associated with inflammation, apoptosis, and the progression of osteoarthritis.[35,36] However, Cer can have a protective role in certain contexts, and a decrease in Cer levels may reflect membrane damage or dysfunction in cellular functions.[37,38] Damaged chondrocytes cannot effectively synthesize or maintain normal levels of Cer. Conversely, when cartilage is injured by external stress, the body attempts to promote the repair of the damaged cartilage tissue by modulating inflammatory responses and cellular protective mechanisms, and the reduction in Cer levels is a manifestation of the body's response to injury.[39] In this study, after damage to chondrocytes, local Cer levels decreased in rabbit cartilage defects, leading to membrane damage or dysfunction that failed to trigger protective mechanisms for cartilage repair. Following scaffold implantation, Cer levels rebounded, enhancing the stability of damaged local chondrocytes and aiding in the repair process.

SMs are synthesized from Cer and phosphatidylcholine via SM synthase (SMS), and the decrease in Cer levels is accompanied by a reduction in SMs.[40] Sox9 is a transcription factor that plays a critical role in cartilage formation and development.[41] As a member of the SRY-box transcription factor (SOX) family, it promotes normal chondrocyte function and development by regulating the expression of cartilage-related genes such as Col2 and biglycan.[42,43] Research shows that SM may influence the role of Sox9 in chondrocytes by regulating the phosphorylation state of transcription factors or intracellular signaling pathways.[44] Conversely, Sox9 may also affect the expression of genes associated with SMS, indirectly regulating the levels of SM.[45,46] Furthermore, during cartilage development, Sox9 maintains the balance of cartilage by regulating cellular growth and apoptosis. Sox9 promotes the survival of chondrocytes and can inhibit excessive apoptosis.[42] Col2 is the main component of the cartilage matrix, and its degradation products are commonly used as biomarkers for cartilage injury and diseases like osteoarthritis.[47] Col2 interacts with integrins, influencing cellular signaling pathways. Changes in membrane sphingolipids can affect integrin dynamics, thereby impacting cell adhesion and

migration.[48] The expression of Sox9 is crucial for the synthesis of Col2 during cartilage development. Sox9 promotes transcription by directly binding to the promoter region of the Col2.[49,50] A lack of Sox9 leads to reduced expression of Col2, affecting the normal formation and function of cartilage.[51] Our findings demonstrated that scaffold implantation inhibited apoptosis of chondrocytes, promoted Sox9 expression, and enhanced ECM repair; additionally, it restored disrupted lipid metabolism in cartilage tissue to homeostasis, thereby accelerating cartilage repair.

Despite some limitations, including the need for further experimental studies to verify the mechanism of action of the 3D-printed scaffold containing polydatin on lipidomics and apoptosis in cartilage damage, as well as the lack of clinical trials to validate its efficacy, our findings provide new insights into cartilage injury repair. These results serve as foundational experimental evidence for future clinical trials.

5. Conclusion

This study developed a 3D-printed scaffold composed of collagen, sodium alginate, and silk fibroin, loaded with PD, designed to aid chondrocyte adhesion and growth. Upon implantation into rabbit cartilage defects, the scaffold facilitated the restoration of disrupted lipid metabolism to homeostasis, decreased chondrocyte apoptosis, promoted the expression of vascular-related proteins, and supported cartilage collagen matrix remodeling, thereby accelerating cartilage repair.

Acknowledgments

The authors acknowledge the guidance of Professor Yadong Yang from the School of Laboratory Medicine and Bioengineering, Hangzhou Medical College (Hangzhou, China) in the field of 3D printing.

Funding

This research was supported by multiple funds from the following: the National Natural Science Foundation of China (No. 81904053); Zhejiang Provincial Natural Science Foundation of China (No. LTGY24H290006); Zhejiang Province Medical and Health Science and Technology Project (No. 2025KY191); Special Research Project of the Affiliated Hospital of Zhejiang Chinese Medical University (No. 2021FSYYZY43); Hangzhou Science and Technology Planning Project (No. 20220919Y084); Zhejiang Province Traditional Chinese Medicine Science and Technology Project (No. 2023ZR046); and Hangzhou Bio-Medicine and Health Industry Development Support Science and Technology Project (Nos. 2023WJC243 and 2023WJC249).

Conflict of interest

All the authors declare that they have no conflicts of interest.

Author contributions

Conceptualization: Weibin Du, Wenxiang Zeng
Data curation: Weibin Du, Wenxiang Zeng
Formal analysis: Wenxiang Zeng, Zhenwei Wang, Huahui Hu, Yanghua Tang, Wei Zhuang
Funding acquisition: Weibin Du
Methodology: Weibin Du, Zhenwei Wang, Huahui Hu, Yanghua Tang, Gang Qu
Project administration: Gang Qu
Supervision: Guoping Cao, Gang Qu
Validation: Zhenwei Wang, Huahui Hu, Yanghua Tang
Writing–original draft: Weibin Du, Wenxiang Zeng
Writing–review & editing: Guoping Cao, Gang Qu

Ethics approval and consent to participate

The purchase, feeding, and other animal procedures followed the animal research guidelines of the National Institute of Health and the Animal Research Committee. All animal experiments were approved by the Experimental Animal Ethics Committee of Zhejiang Chinese Medical University (No. IACUC-20231030-14).

Consent for publication

Not applicable.

Availability of data

All data generated and/or analyzed during this study are included in this published article.

References

1. Paul S, Schrobback K, Tran PA, et al. GelMA-glycol chitosan hydrogels for cartilage regeneration: the role of uniaxial mechanical stimulation in enhancing mechanical, adhesive, and biochemical properties. *APL Bioeng*. 2023;7(3):036114. doi: 10.1063/5.0160472

2. Wei W, Ma Y, Yao X, et al. Advanced hydrogels for the repair of cartilage defects and regeneration. *Bioact Mater*. 2020;6(4):998-1011. doi: 10.1016/j.bioactmat.2020.09.030

3. Liu YY, Intini C, Dobricic M, O'Brien FJ, LLorca J, Echeverry-Rendon M. Collagen-based 3D printed poly (glycerol sebacate) composite scaffold with biomimicking

mechanical properties for enhanced cartilage defect repair. *Int J Biol Macromol*. 2024;280(Pt 2):135827.
doi: 10.1016/j.ijbiomac.2024.135827

4. Peng L, Li H, Deng H, et al. Combination of a human articular cartilage-derived extracellular matrix scaffold and microfracture techniques for cartilage regeneration: a proof of concept in a sheep model. *J Orthop Translat*. 2023;44: 72-87.
doi: 10.1016/j.jot.2023.09.004

5. Li H, He Z, Li W, et al. Exploring the mechanism of microfracture in the treatment of porcine full-thickness cartilage defect. *Am J Sports Med*. 2023;51(4):1033-1046.
doi: 10.1177/03635465231153630

6. Huang Z, Liu C, Zheng G, et al. Articular cartilage regeneration via induced chondrocyte autophagy by sustained release of leptin inhibitor from thermo-sensitive hydrogel through STAT3/REDD1/mTORC1 cascade. *Adv Healthc Mater*. 2023;12(30):e2302181.
doi: 10.1002/adhm.202302181

7. Lee KW, Chung K, Nam DH, Jung M, Kim SH, Kim HG. Decellularized allogeneic cartilage paste with human costal cartilage and crosslinked hyaluronic acid-carboxymethyl cellulose carrier augments microfracture for improved articular cartilage repair. *Acta Biomater*. 2023;172: 297-308.
doi: 10.1016/j.actbio.2023.10.008

8. Migliorini F, Maffulli N, Baroncini A, et al. Allograft versus autograft osteochondral transplant for chondral defects of the talus: systematic review and meta-analysis. *Am J Sports Med*. 2022;50(12):3447-3455.
doi: 10.1177/03635465211037349

9. Wang AS, Nagelli CV, Lamba A, Saris DBF, Krych AJ, Hevesi M. Minimum 10-year outcomes of matrix-induced autologous chondrocyte implantation in the knee: a systematic review. *Am J Sports Med*. 2024;52(9):2407-2414.
doi: 10.1177/03635465231205309

10. Chen R, Pye JS, Li J, Little CB, Li JJ. Multiphasic scaffolds for the repair of osteochondral defects: Outcomes of preclinical studies. *Bioact Mater*. 2023;27:505-545.
doi: 10.1016/j.bioactmat.2023.04.016

11. Shaygani H, Mofrad YM, Demneh SMR, Hafezi S, Almasi-Jaf A, Shamloo A. Cartilage and bone injectable hydrogels: a review of injectability methods and treatment strategies for repair in tissue engineering. *Int J Biol Macromol*. 2024; 282(Pt 2):136689.
doi: 10.1016/j.ijbiomac.2024.136689

12. Cheah CM, Chua CK, Leong KF, Chua SW. Development of a tissue engineering scaffold structure library for rapid prototyping. Part 1: investigation and classification. *Int J Adv Manuf Technol*. 2003;21:291-301.
doi: 10.1007/s001700300034

13. Cheah CM, Chua CK, Leong KF, Chua SW. Development of a tissue engineering scaffold structure library for rapid prototyping. Part 2: parametric library and assembly program. *Int J Adv Manuf Technol*. 2003;21: 302-312.
doi: 10.1007/s001700300035

14. Du J, Zhu Z, Liu J, et al. 3D-printed gradient scaffolds for osteochondral defects: current status and perspectives. *Int J Bioprint*. 2023;9(4):724.
doi: 10.18063/ijb.724

15. O'Shea DG, Hodgkinson T, Curtin CM, O'Brien FJ. An injectable and 3D printable pro-chondrogenic hyaluronic acid and collagen type II composite hydrogel for the repair of articular cartilage defects. *Biofabrication*. 2023;16(1): 015007.
doi: 10.1088/1758-5090/ad047a

16. Du W, Wang Z, Han M, et al. Astragalus polysaccharide-containing 3D-printed scaffold for traumatized skin repair and proteomic study. *J Cell Mol Med*. 2024;28(16):e70023.
doi: 10.1111/jcmm.70023

17. Du W, Hu J, Huang X, et al. Feasibility of repairing skin defects by VEGF(165) gene-modified iPS-HFSCs seeded on a 3D printed scaffold containing astragalus polysaccharide. *J Cell Mol Med*. 2023;27(15):2136-2149.
doi: 10.1111/jcmm.17800

18. Gong W, Zhang N, Sun X, et al. Cardioprotective effects of polydatin against myocardial injury in HFD/stz and high glucose-induced diabetes via a Caveolin 1-dependent mechanism. *Phytomedicine*. 2024;135:156055.
doi: 10.1016/j.phymed.2024.156055

19. Zhang Z, Sun Z, Jia R, et al. Protective effects of polydatin against bone and joint disorders: the *in vitro* and *in vivo* evidence so far. *Nutr Res Rev*. 2024;37(1):96-107.
doi: 10.1017/S0954422423000082.

20. Bagheri Bavandpouri FS, Azizi A, Abbaszadeh F, et al. Polydatin attenuated neuropathic pain and motor dysfunction following spinal cord injury in rats by employing its anti-inflammatory and antioxidant effects. *Front Pharmacol*. 2024;15:1452989.
doi: 10.3389/fphar.2024.1452989

21. Ye Z, Lin J, He C, et al. Polydatin protects against articular cartilage degeneration by regulating autophagy mediated by the AMPK/mTOR signaling pathway. *Histol Histopathol*. 2024;39(11):1505-1515.
doi: 10.14670/HH-18-739

22. Tang S, Tang Q, Jin J, et al. Polydatin inhibits the IL-1beta-induced inflammatory response in human osteoarthritic chondrocytes by activating the Nrf2 signaling pathway and ameliorates murine osteoarthritis. *Food Funct*. 2018;9(3):1701-1712.
doi: 10.1039/c7fo01555k

23. Zhao Z, Wang Y, Yin B, et al. Defect-adaptive stem-cell-microcarrier construct promotes tissue repair in rabbits with knee cartilage defects. *Stem Cell Rev Rep*. 2023;19(1):201-212. doi: 10.1007/s12015-022-10421-0

24. Ye C, Chen J, Qu Y, et al. Naringin in the repair of knee cartilage injury via the TGF-beta/ALK5/Smad2/3 signal transduction pathway combined with an acellular dermal matrix. *J Orthop Translat*. 2021;32:1-11. doi: 10.1016/j.jot.2021.06.004

25. Liu H, Liu H, Yang Q, Fan Z. LncRNA SNHG1 enhances cartilage regeneration by modulating chondrogenic differentiation and angiogenesis potentials of JBMMSCs via mitochondrial function regulation. *Stem Cell Res Ther*. 2024;15(1):177. doi: 10.1186/s13287-024-03793-2

26. Yang Z, Li H, Tian Y, et al. Biofunctionalized structure and ingredient mimicking scaffolds achieving recruitment and chondrogenesis for staged cartilage regeneration. *Front Cell Dev Biol*. 2021;9:655440. doi: 10.3389/fcell.2021.655440

27. Hu G, Liang Z, Fan Z, et al. Construction of 3D-bioprinted cartilage-mimicking substitute based on photo-crosslinkable Wharton's jelly bioinks for full-thickness articular cartilage defect repair. *Mater Today Bio*. 2023;21:100695. doi: 10.1016/j.mtbio.2023.100695

28. Kim YB, Lee H, Kim GH. Strategy to achieve highly porous/biocompatible macroscale cell blocks, using a collagen/genipin-bioink and an optimal 3D printing process. *ACS Appl Mater Interfaces*. 2016;8(47):32230-32240. doi: 10.1021/acsami.6b11669

29. Zhou Z, Cui J, Wu S, Geng Z, Su J. Silk fibroin-based biomaterials for cartilage/osteochondral repair. *Theranostics*. 2022;12(11):5103-5124. doi: 10.7150/thno.74548

30. Fang Z, Liu G, Wang B, et al. An injectable self-healing alginate hydrogel with desirable mechanical and degradation properties for enhancing osteochondral regeneration. *Carbohydr Polym*. 2024;343:122424. doi: 10.1016/j.carbpol.2024.122424

31. Fang K, Li P, Zhang B, et al. Insights on updates in sodium alginate/MXenes composites as the designer matrix for various applications: a review. *Int J Biol Macromol*. 2024;269:132032. doi: 10.1016/j.ijbiomac.2024.132032

32. Sanchez-Ballester NM, Bataille B, Soulairol I. Sodium alginate and alginic acid as pharmaceutical excipients for tablet formulation: structure-function relationship. *Carbohydr Polym*. 2021;270:118399. doi: 10.1016/j.carbpol.2021.118399

33. Chaurasia B, Summers SA. Ceramides in metabolism: key lipotoxic players. *Annu Rev Physiol*. 2021;83:303-330. doi: 10.1146/annurev-physiol-031620-093815

34. Hu L, Luo D, Zhang H, He L. Polydatin inhibits IL-1β-mediated chondrocyte inflammation and ameliorates cartilage degradation: involvement of the NF-κB and Wnt/β-catenin pathways. *Tissue Cell*. 2022;78:101865. doi: 10.1016/j.tice.2022.101865

35. Alizadeh J, da Silva Rosa SC, Weng X, et al. Ceramides and ceramide synthases in cancer: focus on apoptosis and autophagy. *Eur J Cell Biol*. 2023;102(3):151337. doi: 10.1016/j.ejcb.2023.151337

36. Armistead J, Höpfl S, Goldhausen P, et al. A sphingolipid rheostat controls apoptosis versus apical cell extrusion as alternative tumour-suppressive mechanisms. *Cell Death Dis*. 2024;15(10):746. doi: 10.1038/s41419-024-07134-2

37. Peche VS, Pietka TA, Jacome-Sosa M, et al. Endothelial cell CD36 regulates membrane ceramide formation, exosome fatty acid transfer and circulating fatty acid levels. *Nat Commun*. 2023;14(1):4029. doi: 10.1038/s41467-023-39752-3

38. Bao HN, Yin J, Wang LY, et al. Aberrant accumulation of ceramides in mitochondria triggers cell death by inducing autophagy in Arabidopsis. *J Exp Bot*. 2024;75(5):1314-1330. doi: 10.1093/jxb/erad456

39. Tu H, YL Li. Inflammation balance in skeletal muscle damage and repair. *Front Immunol*. 2023;14:1133355. doi: 10.3389/fimmu.2023.1133355

40. Adada M, Luberto C, Canals D. Inhibitors of the sphingomyelin cycle: sphingomyelin synthases and sphingomyelinases. *Chem Phys Lipids*. 2016;197:45-59. doi: 10.1016/j.chemphyslip.2015.07.008

41. Haseeb A, Kc R, Angelozzi M, et al. SOX9 keeps growth plates and articular cartilage healthy by inhibiting chondrocyte dedifferentiation/osteoblastic redifferentiation. *Proc Natl Acad Sci USA*. 2021;118(8):e2019152118. doi: 10.1073/pnas.2019152118

42. Lefebvre V, Angelozzi M, Haseeb A. SOX9 in cartilage development and disease. *Curr Opin Cell Biol*. 2019;61:39-47. doi: 10.1016/j.ceb.2019.07.008

43. Song H, Park K. Regulation and function of SOX9 during cartilage development and regeneration. *Semin Cancer Biol*. 2020;67(Pt 1):12-23. doi: 10.1016/j.semcancer.2020.04.008

44. Gilbert SJ, Blain EJ, Duance VC, Mason DJ. Sphingomyelinase decreases type II collagen expression in bovine articular cartilage chondrocytes via the ERK signaling pathway. *Arthritis Rheum*. 2008;58(1):209-220. doi: 10.1002/art.23172

45. Piacentino ML, Fasse AJ, Camacho-Avila A, Grabylnikov I, Bronner ME. SMPD3 expression is spatially regulated in

the developing embryo by SOXE factors. *Dev Biol*. 2024; 506:31-41.
doi: 10.1016/j.ydbio.2023.11.011

46. Lucki NC and MB Sewer. Nuclear sphingolipid metabolism. *Annu Rev Physiol*. 2012;74:131-51.
doi: 10.1146/annurev-physiol-020911-153321

47. Xu Z, Xu B, Lundström SL, et al. A subset of type-II collagen-binding antibodies prevents experimental arthritis by inhibiting FCGR3 signaling in neutrophils. *Nat Commun*. 2023;14(1):5949.
doi: 10.1038/s41467-023-41561-7

48. Zeltz C, Gullberg D. The integrin-collagen connection – a glue for tissue repair? *J Cell Sci*. 2016;129(4):653-664.
doi: 10.1242/jcs.180992

49. Lauer JC, Selig M, Hart ML, Kurz B, Rolauffs B. Articular chondrocyte phenotype regulation through the cytoskeleton and the signaling processes that originate from or converge on the cytoskeleton: towards a novel understanding of the intersection between actin dynamics and chondrogenic function. *Int J Mol Sci*. 2021;22(6):3279.
doi: 10.3390/ijms22063279

50. Renard E, Porée B, Chadjichristos C, et al. Sox9/Sox6 and Sp1 are involved in the insulin-like growth factor-I-mediated upregulation of human type II collagen gene expression in articular chondrocytes. *J Mol Med (Berl)*. 2012;90(6):649-666.
doi: 10.1007/s00109-011-0842-3

51. Simental-Mendía M, Lara-Arias J, Álvarez-Lozano E, et al. Cotransfected human chondrocytes: over-expression of IGF-I and SOX9 enhances the synthesis of cartilage matrix components collagen-II and glycosaminoglycans. *Braz J Med Biol Res*. 2015;48(12):1063-1070.
doi: 10.1590/1414-431X20154732